frontiers | Frontiers in Dental Medicine

TYPE Original Research
PUBLISHED 04 January 2023
DOI 10.3389/fdmed.2022.1066501

Check for updates

OPEN ACCESS

EDITED BY
Marco Bottino,
University of Michigan, United States

REVIEWED BY
Isaac Jordao De Souza Araujo,
University of Tennessee Health Science Center (UTHSC), United States
Nileshkumar Dubey,
National University of Singapore, Singapore

*CORRESPONDENCE
Nicanor I. Moldovan
✉ nimoldov@iupui.edu

SPECIALTY SECTION
This article was submitted to Regenerative Dentistry, a section of the journal Frontiers in Dental Medicine

RECEIVED 10 October 2022
ACCEPTED 02 December 2022
PUBLISHED 04 January 2023

CITATION
Dairaghi J, Benito Alston C, Cadle R, Rogozea D, Solorio L, Barco CT and Moldovan NI (2023) A dual osteoconductive-osteoprotective implantable device for vertical alveolar ridge augmentation.
Front. Dent. Med 3:1066501.
doi: 10.3389/fdmed.2022.1066501

COPYRIGHT
© 2023 Dairaghi, Benito Alston, Cadle, Rogozea, Solorio, Barco and Moldovan. This is an open-access article distributed under the terms of the Creative Commons Attribution License (CC BY). The use, distribution or reproduction in other forums is permitted, provided the original author(s) and the copyright owner(s) are credited and that the original publication in this journal is cited, in accordance with accepted academic practice. No use, distribution or reproduction is permitted which does not comply with these terms.

A dual osteoconductive-osteoprotective implantable device for vertical alveolar ridge augmentation

Jacob Dairaghi[1], Claudia Benito Alston[2], Rachel Cadle[1], Dan Rogozea[1], Luis Solorio[2], Clark T. Barco[3] and Nicanor I. Moldovan[3,4]*

[1]Department of Biomedical Engineering, IUPUI, Indianapolis, IN, United States, [2]Weldon School of Biomedical Engineering, Purdue University, West Lafayette, IN, United States, [3]Department of Dentistry, Richard L. Roudebush VA Medical Center, Indianapolis, IN, United States, [4]3D Tissue Bioprinting Core Laboratory, Indiana Institute for Medical Research, Indianapolis, IN, United States

Repair of large oral bone defects such as vertical alveolar ridge augmentation could benefit from the rapidly developing additive manufacturing technology used to create personalized osteoconductive devices made from porous tricalcium phosphate/hydroxyapatite (TCP/HA)-based bioceramics. These devices can be also used as hydrogel carriers to improve their osteogenic potential. However, the TCP/HA constructs are prone to brittle fracture, therefore their use in clinical situations is difficult. As a solution, we propose the protection of this osteoconductive multi-material (herein called "core") with a shape-matched "cover" made from biocompatible poly-ε-caprolactone (PCL), which is a ductile, and thus more resistant polymeric material. In this report, we present a workflow starting from patient-specific medical scan in Digital Imaging and Communications in Medicine (DICOM) format files, up to the design and 3D printing of a hydrogel-loaded porous TCP/HA core and of its corresponding PCL cover. This cover could also facilitate the anchoring of the device to the patient's defect site *via* fixing screws. The large, linearly aligned pores in the TCP/HA bioceramic core, their sizes, and their filling with an alginate hydrogel were analyzed by micro-CT. Moreover, we created a finite element analysis (FEA) model of this dual-function device, which permits the simulation of its mechanical behavior in various anticipated clinical situations, as well as optimization before surgery. In conclusion, we designed and 3D-printed a novel, structurally complex multi-material osteoconductive-osteoprotective device with anticipated mechanical properties suitable for large-defect oral bone regeneration.

KEYWORDS

3D printing, bioprinting, digital design, mandibular, osteoconductive, osteoprotective, implantable device

Introduction

Oral and maxillofacial reconstruction is required for a variety of intraoral and extraoral critically sized bone defects and is performed on 1.5 million patients worldwide each year (1). These defects can originate from injuries such as a car accident, congenital conditions such as cleft palate, or diseases such as osteosarcoma (2). Such defects frequently lead to dental loss which can affect speaking and eating and potentially psychological effects due to the patient's distorted appearance (3). The current treatment for these patients is the use of dental prostheses that improve masticatory performance and overall patient satisfaction. However, to attain this goal, enough bone volume for dental device placement and structural support for long-term function is needed (4).

Currently one of the most used alveolar augmentation methods is Guided Bone Regeneration (GBR), using either autogenous bone blocks (5), allogenic materials (6), or *de novo* tissue-like graft devices which are placed on the alveolar ridge or in between areas of pedicled bone (7). In all these cases, the graft device must be adapted to the recipient site and immobilized to provide stabilization, which permits integration and re-vascularization (4). Moreover, for successful GBR the grafts should have appropriate biological and mechanical properties, be customized to fit into the bone defect, allow easy fixation (in most cases, by use of screws), have smooth edges, and a tension-free soft tissue closure of the covering flaps (8). A personalized graft shape has many advantages: shorter time of surgery, better healing, reduced risk of complications, higher rate of success, and ultimately improved patient satisfaction.

Traditional bone augmentation requires manually cut, shaped, and formed grafts, which is time-consuming and often heavily dependent on a surgeon's experience and resources. Thus, there is substantial need to customize GBR graft devices with shapes that fit exactly to a patients' local anatomy. For this reason, 3D printing is emerging as a promising method to form bespoke porous and volumetrically stable scaffolds for bone regeneration (9, 10). Computer assisted design/modeling (CAD/CAM) and 3D printing technologies have opened new possibilities to analyze bone defects by 3D imaging, allowing customization of the grafts to the recipient site (8).

These computer-guided technologies have enabled clinicians to evaluate the dimensions of bone defects in a 3D perspective prior to surgery utilizing computerized tomography (CT), or other 3D medical imaging methods (4). The graft can be designed directly using the 3D model, and then the design can be implemented by either 3D printing (10) or milling (8). Materials used for GBR applications must provide sufficient mechanical support to withstand mastication force and be bioresorbable, without causing adverse tissue reactions, and the material should facilitate bone regeneration (11). Bioceramics such as TCP/HA, have a good propensity for osteoinduction (12–15); however, these materials are not mechanically robust enough to withstand masticatory forces when 3D printed (16). In this study we provide the proof of concept for a solution, consisting of confining the osteoconductive "core" material under a mechanically resilient, biocompatible "cover".

Materials and methods

Image sources

Two DICOM images were used in this proof-of-concept study: one was obtained as open source (OS) standard tessellation language (STL) file, and another was an archival deidentified cone CT scan from the Richard L. Roudebush VA Medical Center Dentistry Clinic. The former was downloaded from the NIH 3DPrint Exchange database (Model ID 3DPX-003381, male mandible, European descent, 50–65 years of age, cadaver scan). The latter was processed with 3D Slicer software (https://www.slicer.org/), a free, open source and multi-platform software package for medical, biomedical, and related imaging research, which allows DICOM files from CT scans to be transformed into editable STL models. These files were then imported to Autodesk Meshmixer software (https://www.meshmixer.com/), where bone defects were used to model individualized bone grafts.

Graft device CAD

The devices destined for implantation (herein called "graft devices") were designed and printed following the workflow illustrated in **Figure 1**. In brief, a generic object shape was imported and placed over the missing bone volume. This object was then shaped to conform to the missing volume by sculpting tools within Meshmixer software. A Boolean Difference function was then used to ensure the object had no overlapping volumes with the bone structure. From this new object, a cover was virtually extracted representing a layer of uniform thickness, as also shown in **Figure 2**. This cover was derived from the upper surface of the object using the Hollow function within Meshmixer as well as discarding and bridging tools. The cover was designed to extend past the patient defect to provide an anchoring structure for screws to maintain the graft device placement *in vivo*. During preliminary development, the cover thickness was taken arbitrary, determined by the apparent printability of the material. Later, this parameter was corroborated with values provided by its heuristic mechanical computer model, as

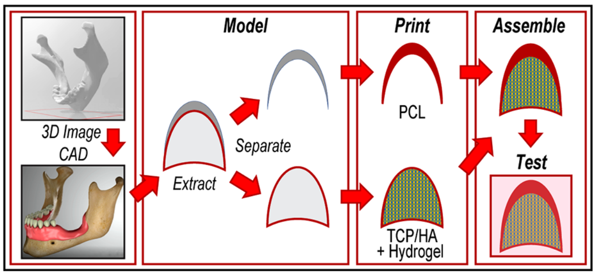

FIGURE 1
Workflow of the current study. From left to right: determination of the missing bone's 3D geometry from DICOM files, followed by extraction of the "cover" and the "core" as separate objects; conversion of these images in printable files, then printing with suitable materials; reassembly of the two portions of the device in one object, and testing of the construct (by computer modeling).

described below. The cover was then also made porous by applying a Tiled Tube pattern within Meshmixer of 1 mm diameter and 2 mm interline distance orthogonal to the surface. The volume remaining after extraction of the "cover" was then used as the template for the "core". This object was also made porous by application of a Lattice Pattern within Meshmixer of 1 mm diameter and 2 mm interline distance, thus creating pores in the X, Y, and Z directions through the core for multidirectional osteointegration.

3D Printing

To verify the printability of the model, preliminary models of both the covers and the cores were printed with a poly-lactic acid (PLA) filament, followed by medical-grade PCL using a Fused Deposition Modeling (FDM) QIDI Tech X-Pro 3D printer (Zhejiang QIDI Technology Co., Ltd, Ruian, P. R. China). For cover generation, Facilan™ PCL 100 filament (3D4Makers B.V., Haarlem, Netherlands) was printed using the 3D printer with settings of: 95°C print temperature, 30°C build plate temperature, 40 mm/s retraction speed, 0.2 mm layer height, 20% infill density, "Grid" infill pattern, 12 mm/s print speed, 35 mm/s travel speed, supports enabled, 60° support angle, "Grid" support pattern, 27% support density, with "print cooling" enabled. To increase print resolution additional cooling was needed due to the slow cooling properties of PCL. To this end, the protective roof and walls of the 3D printer were removed to prevent heat accumulation, and a tube was positioned to provide a constant flow of cool air to the print area. A low print bed temperature of 15–30°C was also utilized to increase the cooling rate of the PCL prints.

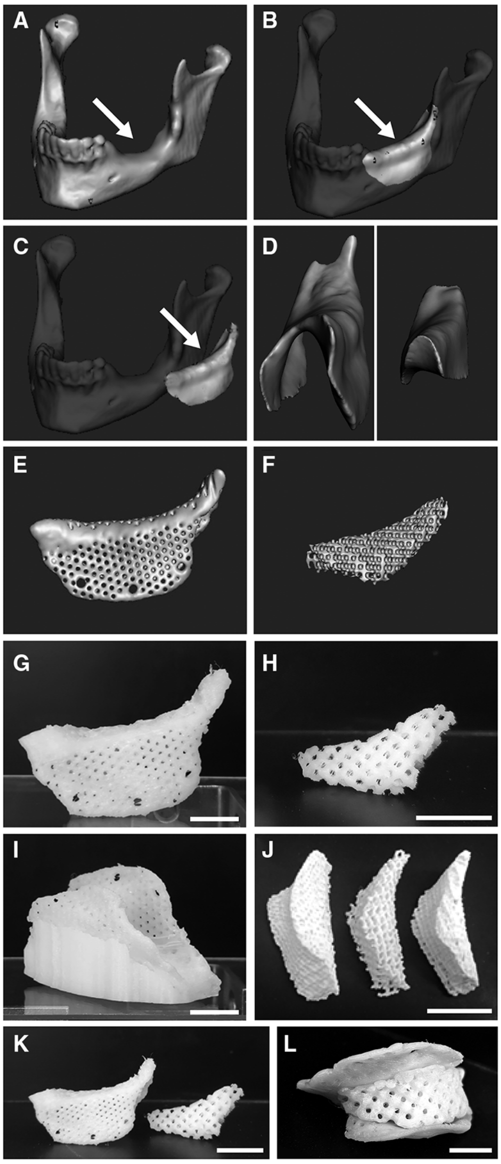

FIGURE 2
CAD and printed graft devices of a large mandibular bone defect. (A–F) CADs. (A) Defect with smooth bone surface (arrow). (B) Empty space leveled at the mandibular ridge to define the graft device (arrow). (C) Defect volume separated as virtual object to be processed individually (arrow). (D) Separation of the cover, representing the upper concave surface of the object (left), from the remaining core (right). (E) CAD of the device's cover, provided with pores and anchoring screws holes. (F) CAD of a porous core. (G–L) Printed constructs. (G) The device's PCL porous cover after removal from the scaffold and smoothing of surface details. (H) Printing of the porous core with PCL (1.5 mm interline distance). (I) Porous cover printed with PCL, shown while still in the co-printed supporting scaffold. (J) Porous cores printed with PLA at three porosities (1, 1.5 and 2 mm interline distance, from right to left). (K) Porous PCL core and porous PCL cover (G,H, respectively) shown here together before assembly. (L) The PCL core fitted into its cover as for surgical placement. Scale bars: (G,I,L), 10 mm; (H,J,K), 15 mm.

Support scaffolds were required due to the device's irregular topography as a result of CAD modeling-driven defect shape. Support scaffolds were generated using QIDI 3D slicer software and were printed using PLA or PCL respectively. Due to over-adherence of supports in PCL models, PCL supports were removed by submerging the scaffold in heated water before removal. The surface was then smoothed by brief local application of chloroform, known to solubilize PCL, to remove any remaining surface inhomogeneities.

For visualization and printing calibration purposes, the core model was initially printed as a solid block with the commonly-used bioink surrogate (17) Nivea paste (from Nivea Creme, Germany). Porous core constructs were then printed using an osteoconductive TCP/HA material (Plotter-Paste-CPC from Innotere GmbH, Radebeul, Germany). This paste was printed using a 0.41 mm inner diameter, conical, plastic tip nozzle on the bioprinter *3DBiofactory* (RegenHU, Villaz-St-Pierre, Switzerland) with the following settings: 3 mm/s feed rate, 20% density, 0.45 needle inner diameter, 0.38 mm layer height, 0.50 mm strand width, and a cartridge airflow pressure of 0.110 MPa. Needle inner diameter settings were set larger than actual needle size to decrease amount of material extruded. This was necessary so that pores did not become blocked due to over-extrusion of the bioink. The printing path for porous TCP/HA constructs was generated using BioCAM software (RegenHU) and utilized a circular print path around individual pores as opposed to commonly used overlapping line patterns (16). This is due to the lattice pattern which was applied to models to create the pores within the CAD model. The porous CPC core was initially printed as the entire model suspended within a hydrogel, but was later sliced into two halves, top and bottom, and printed directly on a glass plate. Both methods utilized a Freeform Reversible Embedding of Suspended Hydrogels (FRESH)-type approach (18), by printing the paste within a support hydrogel (Carbopol 940, from Lubrizol Corp.) as in (19), as we have shown recently (20).

The prints were cured in an electric oven at 75°C for 30–45 min which allowed models to solidify in the desired geometry within the supporting gel. Prints were then extracted from the support gel with a spatula and let dry for 24 h. It was found that objects printed without the use of Carbopol 940 would not solidify when heated under the same conditions and took significantly more time to become solid. Any remaining gel dried to the object was removed by briefly submerging the object in water for rehydration of remaining gel, followed by flushing a jet of water over the object several times from a disposable dropper. The object was then allowed to dry for an additional 24 h.

For objects printed in halves, the two parts were then connected by applying a thin layer of Carbopol to act as a "glue". After reuniting the two halves, the object was placed in an electric oven for 10–20 min at 75°C to dehydrate the gel, resulting in their attachment. This provided the needed stability for assembling the bioceramic-hydrogel construct and the PCL cover for additional testing, while also giving the option to separate the halves (useful e.g., when performing micro-CT analysis) by rehydrating the gluing gel. Otherwise, a surgically approved biocompatible super-glue may be used for permanent attachment of the two halves before surgical placement.

To determine if curing of the TCP/HA followed by re-soaking in hydrogel (as it would happen in a real-life situations) induces the shrinkage of printed constructs, a regular $7.5 \times 7.5 \times 2.5$ mm shape was printed directly on a glass plate, using the same printing settings and the same porosity as the core. On photographs, ten ImageJ measurements were performed to determine the length and width of this object. After printing, Carbopol was applied over this model to allow an accelerated solidification within the electric oven at 75°C, thus replicating the curing process of the core. Similarly, ten ImageJ measurements on photographs taken from the same distance, were performed to determine length and width of the cured construct. The model was then allowed to soak in 4% alginate and crosslinked using 10% $BaCl_2$. A final ten ImageJ measurements were again performed to determine the length and width of the construct.

Hydrogel infusion into the pores

Next, we developed a method to populate the pores of the TCP/HA construct with a biocompatible hydrogel in anticipation of using the hydrogel as a growth factor and/or cells carrier. In order to load the hydrogel within these pores, the solidified structure was soaked in a pre-polymer solution consisting of 4% wt/vol alginate (from Sigma-Aldrich), for approximately 24 h. This pre-polymer concentration was chosen for being less viscous as compared to higher concentrations, which allowed for easier infiltration into the pores by capillarity. Also, preliminary experiments indicated that the self-limiting diffusion depth of crosslinking agents at this alginate concentration is preferable to higher pre-polymer concentrations. The construct was then removed from the pre-polymer solution and submerged in 10% wt/vol of either $CaCl_2$ or $BaCl_2$ for approximately 24 h. For micro-CT analysis, the hydrogel on the surface of the construct needed to me removed, which also extracted it from all the pores closer to the surface. However, both heavy metal atoms also provided enough contrast to clearly show the hydrogel in the deeper pores of the core, based on the acquired x-ray absorbency, besides allowing for the measurement of the actual pore sizes. Although $BaCl_2$ tends to have a shorter/slower diffusion in alginate as compared to $CaCl_2$, it was however preferred for imaging, because of its better visibility in the micro-CT scans (21).

To assess the porosity of the TCP/HA construct and the percent of pores infiltrated by hydrogel, we used sagittal cross sections from reconstructed micro-CT scanning of the porous core with and without loaded crosslinked gel. To this end, the images were imported into ImageJ and converted into an 8-bit image type. An outline was then made around the top and bottom portions of the core individually (since they were printed separately), using the polygon selection tool. Six virtual sections from the micro-CT image at equal distances (three from the top half and three from the bottom half of the core), both from the control and gel sample were selected. The number of pixels at each grayscale values, expressed as Hounsfield Units (HU) (22) was recorded for each selection by use of the histogram function. To account for variation in image size, the number of pixels found at each grayscale value was normalized to the total number of pixels and expressed as percent of total pixels of the image. This way, the percentage of pixels between 0 and 33 HU (black; blank), 34–103 HU (gray; gel), and 104–255 HU (white; scaffold) were determined. These intervals, defined by threshold values, were determined by subtracting the pixel frequencies of the gel sample from the control sample histograms of the core (as illustrated in **Figure 8**). Because the image of the core without gel has contained more pixels up to a grayscale value of 33 HU than the core with gel, we took this as the lower threshold of gel-derived pixels in the micro-CT image. From 34 HU, the image of the core with gel contained more pixels than the core without gel, up to a grayscale value of 103 HU, thus making this the upper threshold of the gel-containing pore images. Then, the fraction of pores infiltrated by hydrogel was calculated by dividing the frequency of pixels between 34 and 103 HU (gray; gel) by the frequency of pixels at or below 103 HU (black/gray), which represented the estimate of available pores for infiltration. Similarly, we determined the overall porosity of the core as the percent of pixels at or below 103 HU (black/gray, representing the total available space of infiltration), from the total pixels associated with the section.

Micro-CT analysis

Two core samples, one with and another without hydrogel, were scanned using a Skyscan 1176 Micro-CT Scanner (Accela, San Ramon, CA). Scans were acquired with a camera resolution of 2,000 × 1,336 pixels, an Al 0.5 mm filter, and 0.50° or 0.80° rotation angle. Due to the size of the object, an "oversized" scan was utilized which combined two scans together to image the entire model. Raw imaging was processed using NRecon software for reconstruction so that further analysis could be performed using software programs including DataViewer, CTan, and CTVox. Models were reconstructed with smoothing enabled (level 2), ring artifact reduction enabled (level 8), beam-hardening correction enabled (20%), and a Gaussian smoothing kernel. Dynamic image range varied between models and ranged between a minimum value of -1500-0HU and a maximum value of 3,000–4,500 HU depending on model density.

Pore size and variation was analyzed by use of "virtual" coronal cross-sections within ImageJ. The scale of the image was set in the software by providing an estimated length of the cross section so that measurements could be converted from pixels to millimeters. The pores were then manually selected, and approximate measurements were obtained by use of an elliptic selection tool within ImageJ. An ellipsoid selection with similar size to each pore was made and the major and minor axis of the selection was averaged to provide an estimated pore diameter. Each of the ten pore diameters were then averaged and the standard deviation was calculated to determine size variance.

Reconstructed data was imported to DataViewer software which was used to display and export coronal and sagittal cross-sections of each scanned model. Alginate gel crosslinked with $CaCl_2$ or $BaCl_2$ appeared with a light gray "hue" when scanned in micro-CT (21). Initial comparison was performed by manually selecting the pores between 2D projections of models either with empty pores or filled with crosslinked hydrogel. The average pixel density was then compared using NIH ImageJ. Gel distribution was further analyzed by inspection of virtual sagittal cross-sections to determine gel distribution throughout the pores of the TCP/HA construct. For better visualization of the hydrogel within the model, a color scale rendering (in inverted mode, for increased contrast) of pixel density was utilized.

3D Scanning

For quantification of the fit of the printed graft device, 3D scanning techniques were employed to determine deviation of the printed PCL cover from the CAD model. Both porous and non-porous PCL cover were 3D scanned. The cover was positioned such that scanning could be performed on the inside of the model. The cover was placed on a rotating scanning board and clay was used to hold the model in place. A high resolution blue light handheld scanner, HandySCAN Black Elite (Creaform, Levis, Canada), was used to 3D scan the printed PCL models. The scan was subsequently exported as an STL file and imported in to Polyworks Inspector (InnovMetric Software Inc, Quebec City, Canada). The original CAD model was aligned to the 3D scan STL using the alignment tool "best fit data to object reference". A colormap was then generated indicating deviation of the 3D scan from the original CAD model from −1.00 to 1.00 mm.

Statical analysis

From the data averages and standard deviations were calculated, and the groups were compared using two-tailed Student's *t*-test. A $p < 0.05$ was considered significant.

Computational modeling

To evaluate how the designed device could withstand mechanical forces, we performed 3D simulations of the force expected on the graft during mastication, using the 3D finite element analysis (FEA) software ANSYS 11.0 (Swanson analysis system, ANSYS, Canonsburg, PA). To simplify the nodes and elements of the model, only the target half of the mandible was considered for the analysis. The model was composed of half of the mandible most pertinent to the graft, the core, the cover, and stand-in models of fixation screws typically used for large defect intraoral bone grafts. Their positions were preliminarily determined by an experienced implantologist (CTB), and were further assessed based on the results of this computer simulation. The stand-in screws were modeled after Pro-Fix Tenting Screws (Osteogenics, Lubbock, TX). The FEA model simulated a 500 N vertical downward load distributed along the top of the alveolar bone ridge, where the masticatory forces are expected to occur, and modeled using the maximum expected force generated by an average human (23, 24). To limit voxel count, only half of the jaw was used in the simulation, and the vertical force was set to 250 N (half the total 500 N force).

Due to the nature of the surgery, patients apply sub-maximal forces during mastication. The expected forces experienced by the graft post-operation were estimated to be approximately 50 N, which is significantly lower than the forces that were modeled. To assure that the device would be significantly robust during regeneration, we designed the device to withstand the maximum expected force for healthy patients (25). The model was fixed along the inferior edge of the mandible assuming forces coming down on the teeth. This creates a comparable situation as when the mandible and maxilla press together during mastication. The mesh was pre-processed in the open-source software MeshLab (developed by ISTI-CNR, Pisa, Italy), to simplify the model nodes to 75% of their original count to increase the speed of the simulation.

The mandible, graft device and screws were considered isotropic, homogenous, and linearly elastic. The material properties were compiled from literature, as shown in **Supplementary Table S1**. The Poisson's ratio of filament-deposited PCL was estimated based on published data and these values were used for our simulation (26–28). Due to the graft being the main area of interest, and the CT-scan having irregular and limited cancellous bone pockets, the whole jaw, including the teeth, were all considered to be from one compact bone-like material. Additionally, the composite core was simplified to be comparable to other hydrogel-hydroxyapatite composites. The stand-in material was TCP/HA, previously shown to have excellent biocompatible (10) and osteoconductive (15) properties. Lastly, the screws were simplified to not possess threading since the threading portion would not be in contact with the graft. The core and cover were simulated as "bonded" contact sets due to the hydrogel core adhering to the inner surface of the cover. To allow for minor displacement and due to the foreign material, the screws were assumed to have a "friction contact" with a coefficient μ of 0.3 between the bone and the screws.

Results

In order to generate our dual-function device, we followed the workflow depicted in **Figure 1**. One of its novelties is the splitting of the CAD model in two distinct parts: one for mechanical protection (called "cover") and one for providing osteogenic activity (named "core"). This approach is here illustrated by graft devices with anatomic representations of mandibular and maxillary defects (**Figure 2** and **Supplementary Figure S4**, respectively).

First, a large mandibular defect presenting a smooth interface at the bone level was found as an open source STL file (**Figure 2A**). To define the graft device, this was further processed by leveling at the mandibular ridge to virtually fill the space (**Figure 2B**). This filling was separated and processed individually (**Figure 2C**), and the upper concave surface of the object was extracted as representing the cover (**Figure 2D**, left), while the remaining volume was used as the core (**Figure 2D**, right).

Then the cover was modeled in varying (arbitrary at this stage) thicknesses (**Supplementary Figure S1A**). To determine their printability, we initially printed the cover with a polylactic acid (PLA) filament at: 1 mm (**Supplementary Figure S1B**), 1.5 mm (**Supplementary Figure S1C**) and 2 mm (**Supplementary Figure S1D**). This test showed that despite their irregular geometry, all these versions of the cover were printable with geometric fidelity and structural robustness. Because of the benefit for biochemical communication *via* nutrients, growth factors, and other important biochemical components, between the osteoconductive core with the tissue flap on top of the device (29), the cover design was modified to exhibit porosity, with pores of 1 mm placed at 2 mm distance (**Figure 2E** for CAD, and **Figure 2G** for the respective printed cover).

Large, uniform and aligned pores were also introduced in the core for easier hydrogel penetration and subsequent migration of bone-derived cells after eventual placement in the mandibular defect. To this end, the core's CAD was made porous by application of 1 mm wide orthogonal lines separated by 2 mm interline distance (**Figure 2F** for CAD, and Figure **2H** for the respective core printed with PCL). For better control of the printing, this model of the porous TCP/HA core was also designed and printed as composed of two halves.

For 3D printing of the cover, we chose PCL as the preferred material, given its biocompatibility, printability, and good mechanical properties. However, because the irregular shape of the cover, an additional scaffold was required to support it during printing (Figure 2I). Due to the low melting point of PCL, the cover could be easily detached from this support by applying heated water. However, this procedure left behind a few surface inhomogeneities that were removed by local application of chloroform, a good solvent for PCL, to smoothen the top of the cover after separation from the supporting scaffold (as in Figure 2G). To determine printability of the core, this was also modeled in three porosities and initially printed using PLA (Figure 2J). The PCL core and cover (Figure 2K) were then assembled to ensure spatial compatibility of the two device components (Figure 2L).

However, we then had to overcome the challenge of 3D printing of the porous core directly with the osteogenic TCP/HA, which is a viscous paste, and to additionally solidify and extract it from the gel as a self-standing object. To this end, we found as suited to this goal the "embedded bioprinting" techniques, performed in Carbopol, the support hydrogel (Figure 3A). Being inert and transparent, Carbopol hydrogel allowed direct imaging of the suspended object during and after printing (Figure 3B), while also supporting the printing of porous objects with minimal loss of surface detail at the intersection of the component lines. Most importantly, this material resisted heating at 75–100°C, thus permitting the hardening of the paste to allow for removal of the porous structure from the gel as intended. Due to the relatively large size of the graft device, the porous core design was printed in two halves which were solidified, extracted, and assembled resulting in successful development of a porous TCP/HA core model (Figure 3C). Next, the "core" and the "cover" were combined in a finally assembled device (Figures 4A,B), demonstrating a good fitting between the defect implemented in a thermoplastic-printed equivalent for the jaw, with the model made from the bioceramic TCA/HA core (Figure 4C), and the PCL cover (Figure 4D).

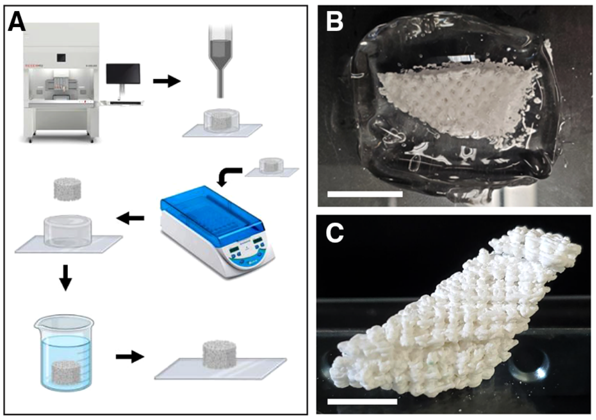

FIGURE 3
Embedded 3D printing of the core with TCP/HA paste. (A) Schematic depicting of the process used for printing and solidification of TCP/HA core (for details, see the Methods section). (B) Half of the TCP/HA core construct printed in Carbopol hydrogel support on a glass slide. (C) The cured, washed, assembled, and re-dried TCP/HA construct. Scale bars: (B,C), 10 mm.

Although this fitting was not yet assessed quantitively in a real-life situation, we could still estimate it based on the covers' printing accuracy. This is because the cover determines the core's available volume which will be composed of both the TCA/HA bioceramic *and* hydrogel, thus occupying any remaining space under the cover. Then it follows that what controls the fitting of the whole device into its intended location is the printing accuracy of the cover. To determine this accuracy, we measured the deviation between the CAD model of both the non-porous (Figure 4E) and porous (Figure 4H) covers and the 3D scans of the non-porous (Figure 4F) and porous printed PCL covers (Figure 4I), respectively. Using this approach, we found that in the considered cases (one compact and one porous), this difference was smaller than 1 mm in all directions (Figures 4G,J and Supplementary Figure S2).

Moreover, we determined that the curing of the TCP/HA followed by re-soaking in hydrogel did not induce a significant modification of the dimensions of the core's material (Supplementary Figure S3). To this end, we created a regular-shape equivalent construct from the same material as the core, and printed it using the same settings. Initially, the length and width of this object were 7.5 ± 0.1 mm and 7.6 ± 0.1 mm, respectively (Supplementary Figure S3A), and these became 7.3 ± 0.2 mm and 7.3 ± 0.1 mm after curing (Supplementary Figure S3B). After soaking in alginate and crosslinking (Supplementary Figure S3C), the length and width were found to be 7.2 ± 0.3 mm and 7.3 ± 0.3 mm, respectively. Altogether, these measurements indicate a −4% change in both directions as compared to the uncured model, as well as a 1% change in length and 0% in width when compared to the cured model. This finding suggests a good preservation of the core's material dimensions during the steps from initial printing to the assembling in the device.

The overall workflow to create the implant device was also applied to a maxillary defect of an actual patient (Supplementary Figure S4A). Because in this case the bone defect was more pronounced and more irregular, the pre-filling of the defect site *in vivo* may be required (Supplementary Figure S4B), before application of our surgically placed device, for which were designed the core (Supplementary Figure S4C) and the cover (Supplementary Figure S4D). Their implementation is shown starting with the CAD viewing from the lingual side (Supplementary Figure S4E) and of the cover-core assembly (Supplementary

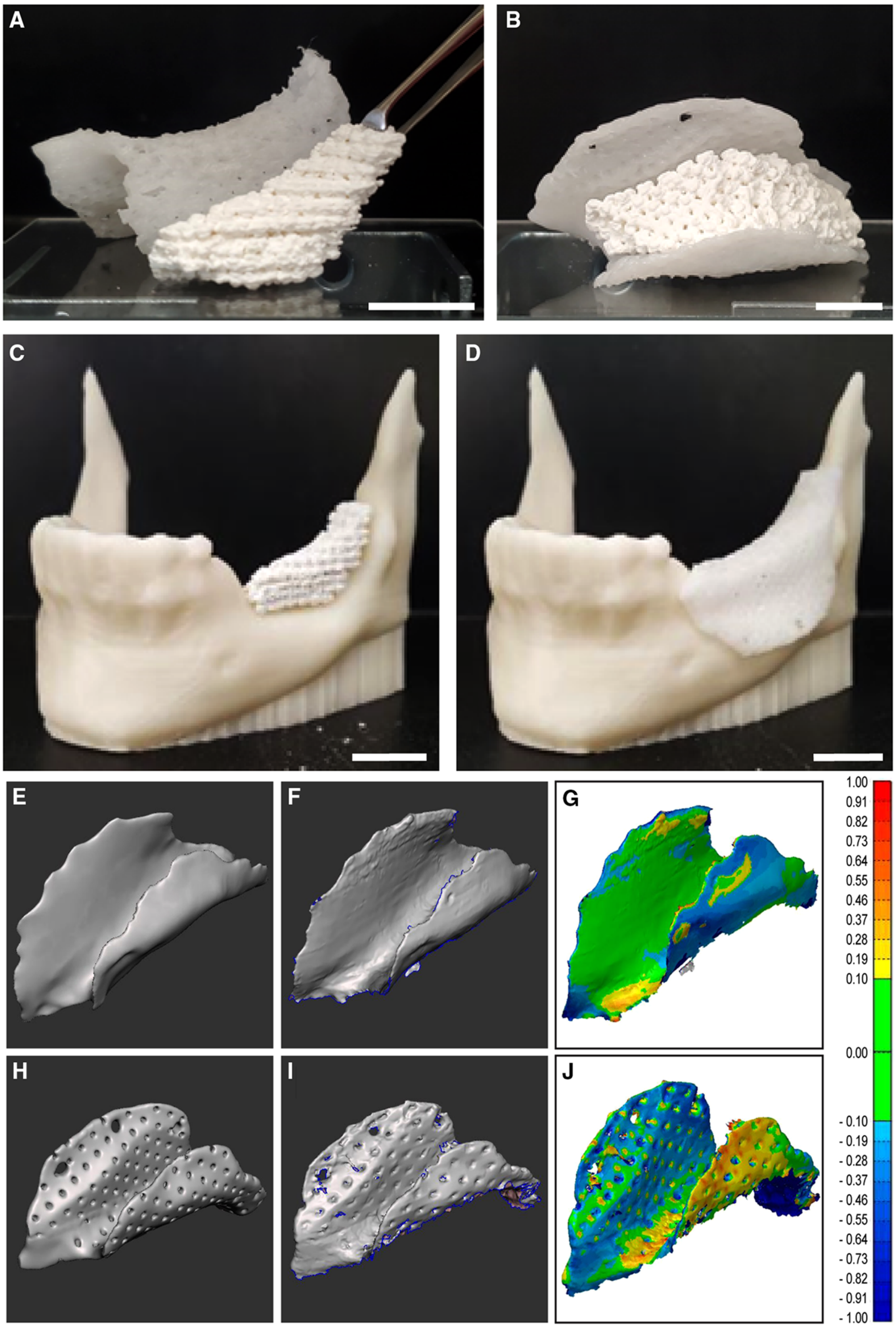

FIGURE 4
Assembling of the core, cover and their computational fitting evaluation. (A–D) Assembly of the printed devices. (A) Osteoconductive porous TCP/HA core next to a PCL cover. (B) The TCP/HA core fitted into its PCL cover as for surgical placement. (C) The TCP/HA core placed in a model of mandibular defect, 3D printed with thermoplastic acrylonitrile butadiene styrene (ABS) polymer. (D) The PCL porous cover placed over the bioceramic core, on the ABS plastic model of the mandibular defect. (E–J) Analysis of the device cover's spatial deviation from its initial CAD. (E,H) CAD of compact and porous cover models, respectively. (F,I) Corresponding virtual equivalents of the printed objects, obtained by 3D scanning. (G,J) The results of the subtraction of one shape from the other (color coded for the amplitude of difference on the right-side scale, in mm). See also Supplementary Figure S2 for additional views. Scale bars: (A,C,D), 15 mm; (B), 10 mm.

Figure S4F), as well as its printing with a PCL cover and a porous TCP/HA core (**Supplementary Figure S4G,H**).

The presence, distribution, and size of the pores inside the 3D printed TCA/HA core were determined by micro-CT (**Figure 5**). Pore size sampling on the images indicated an average value of 0.81 ± 0.08 mm, again in good agreement with the expected size of 1 mm, based on the virtual model. We also sought to determine the presence of the hydrogel *within* the pores of the bioceramic core. This was printed as described, sequentially infused with alginate solution by capillarity, and then crosslinked by the secondary diffusion of the crosslinker. To this end, micro-CT was used in sagittal cross-sectional viewing mode, applied to the construct with empty pores (**Figures 6A,C**), and to that filled with crosslinked alginate (detectable due to the x-ray absorbency of the crosslinker) (**Figures 6B,D**), both in gray scale (**Figures 6A,B**) and in color scale for better visualization (**Figures 6C,D**).

Average percent of gel occupancy within the pores in the sagittal cross section micro-CT images was determined for both the control and the gel-filled samples, using the procedure described in **Methods** (Section 2.4). To determine the threshold grayscale values of the gel-derived pixels, we performed the difference between the histogram of normalized pixel frequencies in the control sample (**Figure 6E**) and that of gel-filled sample (**Figure 6F**). This subtraction generated **Figure 6G**, which allowed us to assign the pixels in the ranges 0–33 HU ("black"), 34–103 HU ("gray"), and 93–255 HU ("white") to the empty pores, gel-filled pores and to the TCP/HA material, respectively, with the aggregated pixel values in these intervals displayed in **Figure 6H**. From here, we calculated that in the alginate-containing core (second column in the 34–103 HU range), the gel-derived pixels represented in average 85 ± 4% ($n = 6$, representing six section planes) of total pixels in the pores (sum of second columns in the 0–33 HU and 34–103 HU range), which is an estimate of pore gel occupancy, in good accord with the color-based evaluation in **Figure 6D**. We also noted in the 34–103 HU pixel range of the hydrogel-free sample a high background (of yet unknown origin); however, being significantly lower than the corresponding values in the hydrogel-loaded sample, and inconsistent with the color-coded image in **Figure 6C**, we concentrated on the gel-containing sample instead. At the same time, the average bioceramic-derived pixels (columns in the 93–255 HU range) amounted to 37 ± 4% ($n = 6$) for the control and 35 ± 2% ($n = 6$) for the hydrogel-loaded sample, of the total pixels respectively, representing a good estimate of the porous core's overall porosity (**Figure 6H**, difference non-significant).

Moreover, we developed a mechanical simulation model of the open-source model using ANSYS, to analyze the effect of device's design on its surface displacements under stress, as well as the risk of microfracture or overt yielding, determined by von Mises stress assessment (30). We modeled the device cover as made of PCL (with an initial thickness of 0.85 mm) and placed three screw holes on the buccal side to anchor it to the mandible. The initial model also had screws placed only on one side, to minimize the time and effort of surgical screw placement and the discomfort to the patient. The screw holes were incorporated directly to the print design, to prevent the possibility of crack propagation in the cover due to subsequent screw insertion *in vivo*. In this case, the

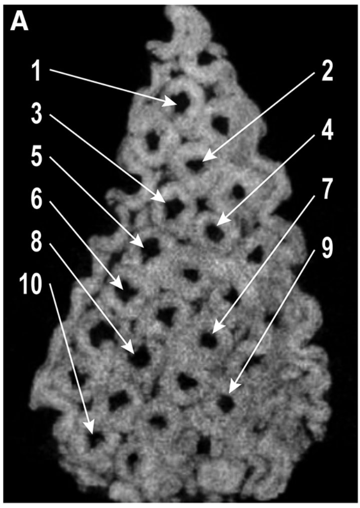

B

Pore number	Major axis (mm)	Minor axis (mm)	Average diameter (mm)
1	0.781	0.781	0.781
2	0.722	0.675	0.698
3	0.880	0.786	0.833
4	0.904	0.904	0.904
5	0.893	0.845	0.869
6	0.893	0.845	0.869
7	0.739	0.611	0.675
8	0.888	0.888	0.888
9	0.880	0.786	0.833
10	0.786	0.730	0.758
	Average:		0.811 ± 0.079

FIGURE 5
Measurement of pore sizes in a 3D printed TCP/HA sample by micro-CT. (A) The coronal cross-section from micro-CT image indicating the pores selected for measurement. (B). Corresponding pore dimensions, as determined by ImageJ analysis.

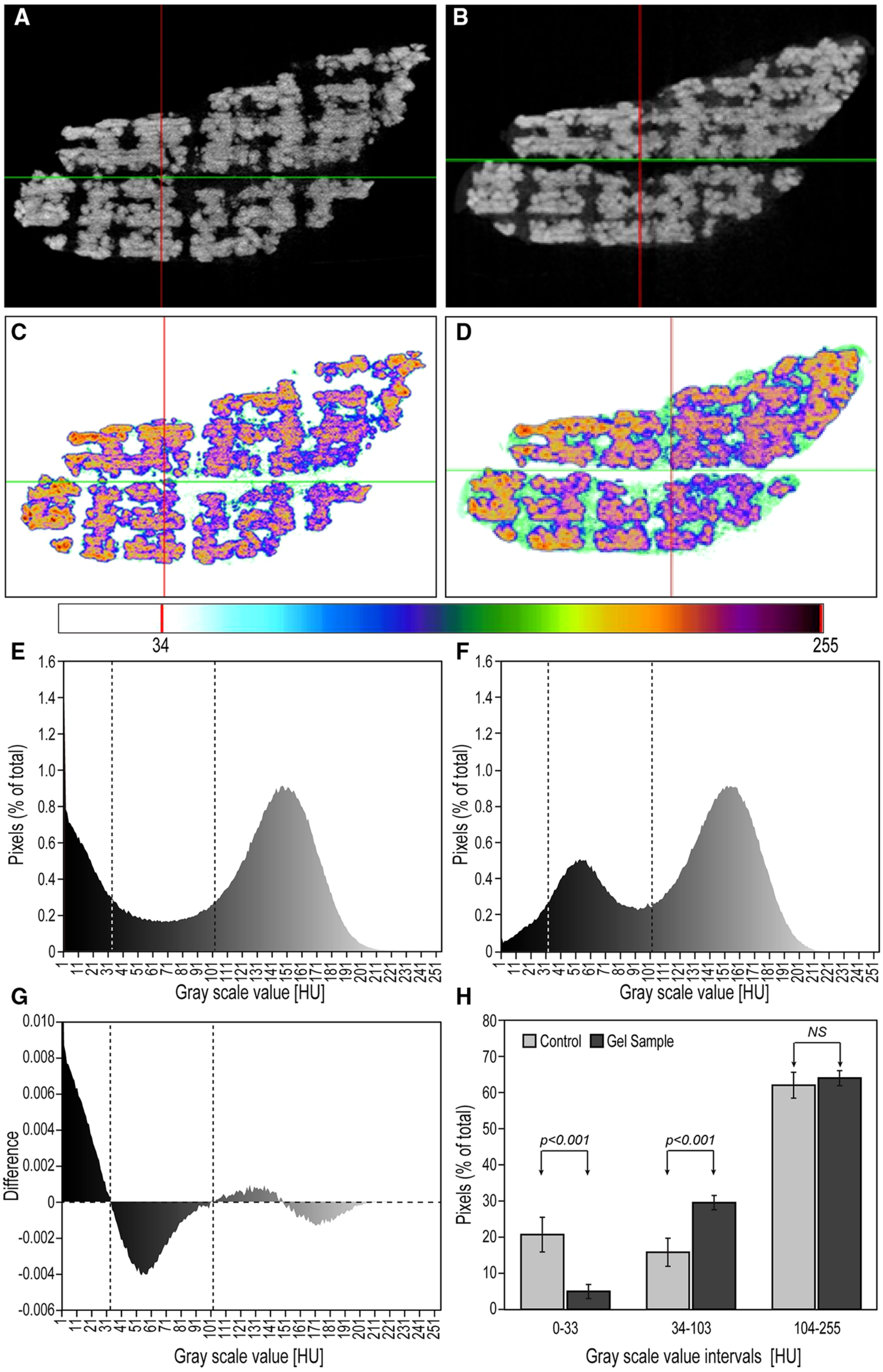

FIGURE 6
Assessment of hydrogel penetration within pores. (A,B) Gray-scale images of the micro-CT scans of non-crosslinked and CaCl$_2$-crosslinked cores, respectively (light gray hue in the pores indicates gel presence). (C,D) Inverted-color images of the micro-CT scans of non-crosslinked and cross-linked cores (greenish/azure color represents the hydrogel). (E,F). Histograms of the number of pixels per gray scale value in empty (E) and gel-filled (F) reconstructed, comparable, sagittal micro-CT cross sections (vertical lines taken from G). (G) Histogram of the difference in pixel frequency between (E), and (F) as dependent on their grayscale distribution, which identifies three regions: empty pores (left), gel-occupied pores (center) and bioceramic-occupied area (right). (H) Bar graphs of the average (±SD) pixel numbers in the three regions identified in (G) (n = 6).

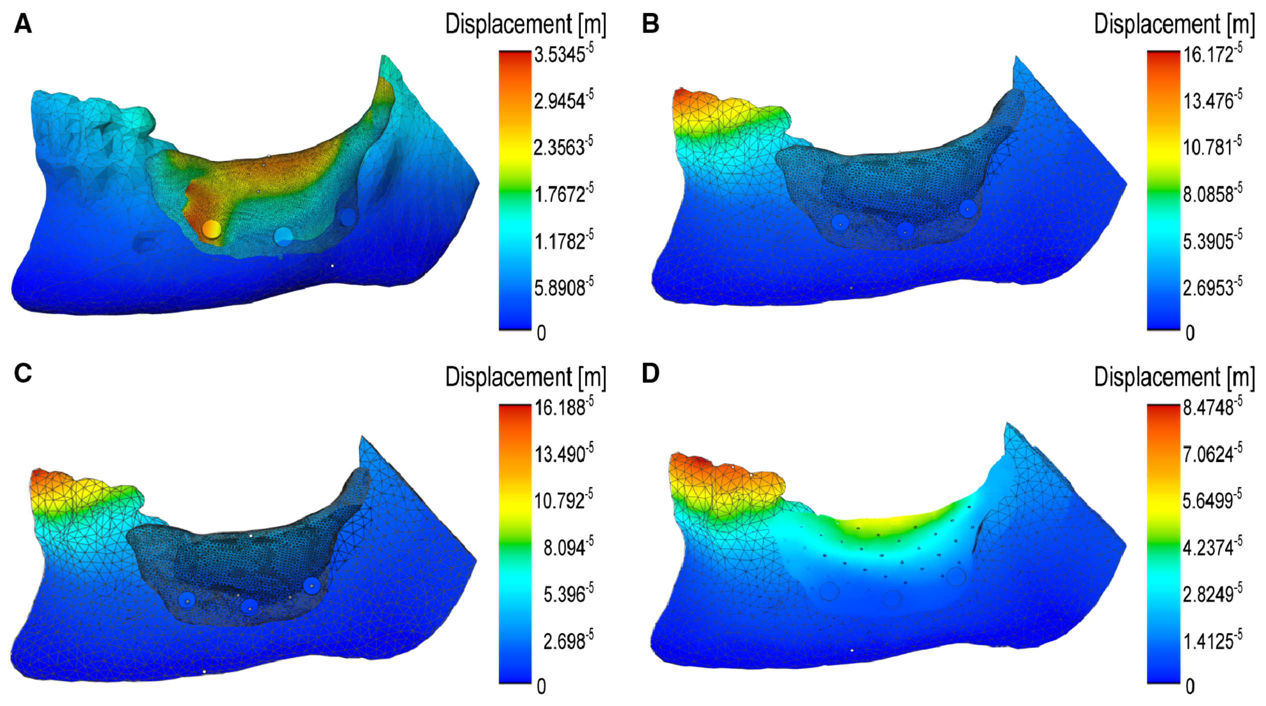

FIGURE 7
Computer modeling of surface displacements under masticatory force on the mandible and on the surgically placed device. (A) Large displacements over a thin (0.85 mm), compact PCL cover immobilized by facial screws: note their mostly lateral localization. (B) Much smaller surfaces displacements on the thicker (1.00 mm) compact cover. (C) Similar surface displacements of the cover after fixing with both facial and lingual screws. (D) Larger but uniform distribution of the surface displacements of the porous cover, fixed with facial screws.

maximum predicted displacement in the cover was located at the top ridge of the cover and at the leftmost screw (Figure 7A), and not expected to buckle under maximum loading conditions according to the von Mises stress values. This indicates that the screws can maintain the cover in place at its location, while allowing for only minor displacement. However, to make the cover's mechanical response to masticatory forces more uniformly distributed, we increased its thickness to 1 mm and indeed, the surface displacements became smaller and much more uniform (Figure 7B). Next, we also assessed the changes brought by the addition of screws on the lingual side of the mandible and found a similar distribution of local displacements (Figure 7C), which confirmed the previous option for fewer screws. Lastly, we analyzed the effect of providing the cover with 0.25 mm pores, and again found a uniform distribution of the displacements, although slightly higher than in the compact case (Figure 7D). In order to determine if the introduction of these pores, as well that of the screws, results in a mechanical failure of the cover during mastication, we analyzed the Von Mises stress distribution, which predicts the yielding at any location on the model (31). Reassuringly, in none of these considered conditions the surface distribution of von Mises stress attained concerning values (Figure 8).

Discussion

Bone grafts are used in medical practice to the benefit of millions of American patients in need for restorations required as a result of congenital defects, trauma, cancer, or other forms of skeletal damage. These grafts are made either from natural bone, or increasingly from biocompatible materials, as we gain a better understanding of the body's response to their properties, to the incorporated extracellular matrix components, and to the use of cellular constituents (32).

Due to their inorganic composition similar to that of the bone, bioceramics are becoming the elective materials for bone regeneration. Based on their interaction with the nearby tissues, bioceramic materials can be classified as bioinert, bioactive (surface-reactive), or bioresorbable. An active line of investigation has been to upgrade the bioactive materials with biomolecules or inorganic ions, useful for bone tissue engineering (33). To provide tissue ingrowth, most bioceramics are porous or are intentionally made porous, as their degree of porosity affects the mechanical and biological properties, particularly when macro- and micro-pores coexist (34). However, this makes them intrinsically brittle, which limits their capability to sustain multiple biomechanical loads. Therefore, the applications of bioceramics were also limited,

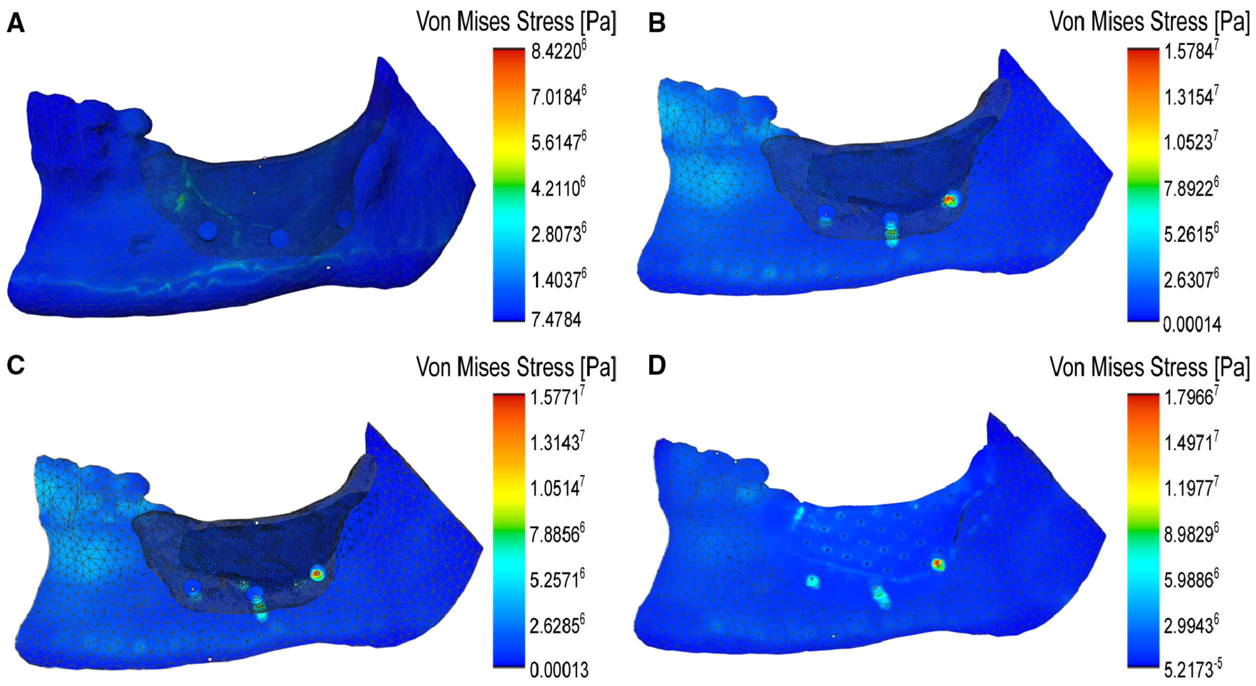

FIGURE 8
Modeling of the distribution of von Mises stresses on the covers under masticatory forces. (**A**) Localized stress maxima on the thin cover. (**B**) Distribution of stresses on the compact cover with three facial anchoring screws. (**C**) Similar distribution of stresses over the cover with both facial and lingual screws. (**D**) Simulation of the von Mises stress distribution over the porous cover model with facial screws. In all situations, note the transfer of stress from the cover to the inferior body of the mandible, where the anterior tensile strains are found.

mainly as grafting materials for the filling of small bone defects. For this reason, efforts are been made to enhance their strength and toughness, by adding organic polymers or other ingredients to control their nanoscale-level structure (35), thus becoming composite bioceramics (36). This could solve some of the mechanical issues of the bioceramic materials, however this still does not guarantee that they will be robust enough to be fixed in place with screws and/or retain their structure in long term surgical placement and may generate new biocompatibility complications. Therefore, to take a full advantage of the beneficial properties of bioceramics, there is a critical need to find a solution for their brittleness. One solution could be our approach of "caging" them under a protective, mechanically resistant cover, which itself can be fixed in place with screws.

Among the biomaterials used for bone tissue engineering, calcium orthophosphates such as TCP/HA belong to the categories of bioresorbable and bioactive compounds (37). In the area of oral bone graft devices, bioceramic TCP/HA provided with a porous structure by 3D printing was shown to induce bone growth and eventually the replacement of mandibular grafts made from this material with new bone (13, 14).

In order to protect the brittle constructs made from TCP/HA, in this study we developed the concept of "cover-core" osteoprotective-osteoconductive, dual function graft device. The "cover" was designed in a defect-specific manner directly from patient scans (DICOM images) and generated by 3D printing from the biocompatible material PCL. Depending on chemistry, geometry and environment (38), a PCL implant is expected to degrade much slower than the core. After 6 months *in vivo*, the degradation was found to be 1% of the initial PCL scaffolds [partially explained by an active recrystallization process (39)], or in another study over 2 years for decomposition (40). Importantly for our project, during degradation the scaffolds retained very well their mechanical properties (41).

For the core made primarily of porous TCP/HA, it could take 6–18 months to be absorbed (42), also depending on the contribution of a chemically crosslinked hydrogel (12). The degradation of physically crosslinked alginate hydrogels may vary depending on their molecular composition and crosslinking. *In vitro*, this is between two (43) and four (44) weeks. This time could be sufficient *in vivo* for deploying their load of cells and/or active biomolecules in the target bone defect, while being slowly replaced with a locally generated fibrin-based hydrogel, cells, and minerals (45).

Combined, these premises established a method for the custom design of a personalized grafting device for alveolar augmentation procedures. Similar workflows for 3D printing of patient—specific grafts for large volume bone regeneration have been published before, using either extrusion bioprinting (9, 10, 46) or laser stereolithography (47). Towards this goal materials such as resorbable porous PCL (9), PCL/TCP paste combined with hydrogel (48), porous HA loaded with cells (49), or bi-material printing of TCP with growth factor-loaded alginate hydrogels (50) have been considered. For these reasons, the preparation of porous bioceramics by additive manufacturing has received increased attention, starting with the design and printing of interconnected pores (51), adjusting the pore size of printed TCP scaffolds to the graft surgical site (16), the *in silico* and *in vivo* mechanical evaluation of the bioprinted scaffold following recellularization (52), or the influence of saliva on surface properties of 3D printed dental devices made for rapid osseointegration (53). For comparative purposes, of particular importance is the patient defect-specific 3D design and printing with TCP/HA, a solid material as recently proposed (10), but also the dual ink strategy with TCP/HA for 3D printing of *in vitro* prevascularized bone scaffolds (12), or similarly with a human bone powder-based bioink (54).

The novelty of our research consists not only in the multimaterial composition of this graft device, but equally importantly in its dual structural organization, containing a fragile (porous) bioceramic-hydrogel core, protected by a solid cover. From the virtual model of the personalized design, we first virtually separated a minimally thick cover while still maintaining capability of sustaining mechanical stresses encountered during mastication (55), and also endowed it with large pores, which would be anchored in the mandibular or maxillary bones through screws.

The large pores of this cover are a critical feature of our design, that will allow important soluble factors and periosteal regenerative cells (56, 57), possibly derived from a purposedly *in situ* generated tissue flap. In fact, additional tissue is needed to cover the graft device to promote post-surgery tissue repair and integration of the bone graft. In this regard, our team has pioneered the formation of this tissue flap by injection of an osmotically expanding material, which builds intra-tissue volume due to fluid adsorption, and thus obliges the covering cellular layer to slowly expand (58–60). This “expander” hydrogel is then extracted, and the overlying tissue flap is used for covering the inserted bone graft.

The device’s core was also designed to contain large, linearly aligned pores in order to promote osteo-conduction (13, 51), to facilitate mass transport and support for plasmatic imbibition, as well as the blood vessel formation (12). We successfully printed it first using the polymeric PCL, given the previous consideration of this material for maxillary implants either alone (9) or in combination with TCP (61), and then with the TCP/HA paste. For this, we adapted an “embedded printing” method in the supporting hydrogel Carbopol (19), for which we also performed technical improvements, such as high temperature backing of the construct in Carbopol (thus reducing the curing time from four days to thirty minutes), followed by its removal as a powder (20).

We also probed whether the porous TCP/HA core can be loaded with alginate, the biocompatible hydrogel commonly used as carrier for cells with regenerative potential (62), and/or with growth factors (63). Thus, the next phase of our research consisted of infusing hydrogels into the porous bioceramic constructs. In principle this is possible either by loading the pores with viscous materials during construct generation (12), or post-printing (64). In practice, we relied on the process of capillary adsorption of the alginate solution in the construct’s large pores, followed by diffusion of the crosslinking agent. This was also useful for hydrogel visualization in micro-CT, due to the x-ray absorption by the heavy metal atoms Ca and Ba used for crosslinking (21).

The micro-CT imaging was also used to characterize the pores diameters, found to be close to that of the virtual design, although slightly smaller given the expected shrinkage due to TCP/HA paste solidification. However, this did not affect much the overall linear dimensions of the construct, which remained within five percent of the original CAD. The printing precision of the solid and porous cover was determined to be within 1 mm of the original CAD model. This is important as the cover would determine the geometry of the core and thus controls the accuracy of the graft device fit to the defect site. Therefore, given that the dimensions of the cover modeled here are in the centimeter range, and the difference with the CAD less than ten percent (or even smaller in reality, due to the possible plastic deformations accumulated by the PCL material during pre-scanning manipulation), the accuracy of the printing ensues to be better than ninety percent. Therefore, we expect that this precision to be also applicable to the fitting of the printed cover when placed in the mandibular bone defect (counting on the concordance between this physical space and its virtual 3D image based on the CT scan, from which derives the printed object).

Based on the analysis of micro-CT images, we estimated the overall space occupied by the bioceramic material to be about 36%, meaning that approx. 64% cross-sectional area was empty. This is a lower value, but close to what is expected for the porosity of mandibular trabecular bone (65). Of note, the pores in our construct are large (of about 0.8 mm) and linear, rather than small and random as in many other synthetic bone-like materials, and thus closer to the trabecular bone morphology.

The image analysis of micro-CT sections also allowed us to estimate the diffusion-driven (followed by crosslinking) alginate hydrogel pore occupancy to be about 85%. However, the pixels between 34 and 103 HU in the control sample, representing a background, were not considered in this calculation because it was not corroborated by its color-coded image. This suggests that there are “background” micro-CT grayscale pixels between these values, due to more than simply the crosslinked gel, whose origin requires further investigation. However, an alternative method for calculation of hydrogel infusion could be to sensitively measure the weight of the bioceramic scaffold before and after loading with hydrogel, then based on its density to determine the volume of the hydrogel retained within the scaffold.

To address the mechanical behavior of the graft device, we generated a finite element analysis model of the device and the surgical site, and simulated their coordinated displacements and stresses under the expected masticatory forces. Through this computer model, a weakness was found in the initial cover design, allowing us to modify the design prior to printing it. Then the predicted displacement in the porous cover model was found to have a maximum occurring at the mandible and screws level. When a functional mandible was simulated under mastication, the peak compressive stress locations was found to be at the inferior body of the mandible, as known from the literature (66). Additionally, there were no localized or exaggerated von Mises stresses, indicating that the mastication would not cause the cover to be forced past its yield point, both in the compact and porous versions.

Thus, our computer model showed that the design and implementation of the PCL cover over a TCP/HA core could effectively sustain a maximum chewing force, even though that would not occur until complete osteointegration. It is important to note that the porous design is not only operating as if it were intact bone, but the maximum von Mises stress occurs at the screws, allowing the force to propagate down through the implant to the defect. This limits the “stress shielding”, a common issue with bone grafts that may lead to a poorly regenerated bone, due to the needed osteogenic effect of mechanical stress, which a too stiff implant tends to eliminate (67). Thus, a porous cover is a viable design option that provides structural protection to the osteoconductive core and may also assist the intended infiltration of humoral and cellular factors from the tissue flap, further assisting the underneath core’s osteointegration.

Among the limitations of this study are the following: (i) we primarily address the conceptual (design) and structural components of the device, but less the functional characterization of device’s components. However, this study pairs well with the recently published paper by (10), who in a similar context, performed the *in vitro* evaluation of the same porous TCP/HA in interaction with stem cells; (ii) we did not yet perform direct mechanical evaluation of this device, which will also be useful for the computational model’s calibration; (iii) therefore, this model is still in the heuristic (i.e., thought-orienting) rather than translational stage.

In the future, we plan to assess this device *in vivo*, from both structural and functional points of view: (i) structurally, this could be done by its retrieval at various intervals from a critical size defect in rats, to determine the cover’s status and the core’s ossification by CT scans, weighting, and immunohistology (which will also give mechanistic insights about its resorption); (ii) the functional characteristics will be addressed both directly and indirectly. Direct characterization may be performed by determining the ability of the new mandibular bone to withstand tooth impanation. In addition, an indirect approach may involve taking advantage of the device’s protected space under the cover which may wirelessly connect mechanical (pressure) and biochemical (pH) sensors to a remote receiver for evaluation of the masticatory function in large animal models of mandibular or maxillary defects.

In conclusion, we demonstrated a comprehensive workflow for a personalized graft device design and 3D printing based on DICOM image reconstructions of patient-specific defects. In addition, we introduced a novel design of a device for vertical bone augmentation containing brittle osteoconductive materials. Because fragile bioprinted graft devices manufactured using osteoconductive materials may disintegrate after surgical placement and do not permit direct anchoring to the underlying bone, here we proposed and demonstrated a “cover-and-core” design. The cover is useful to anchor and protect the osteoconductive core in a vault-shaped, biocompatible polymeric (PCL) material. In order to further stimulate bone ingrowth, this was designed from a composite material containing the osteoconductive TCP/HA porous matrix, coated with a soft hydrogel (crosslinked alginate), which can be used as vehicle for bioactive factors delivery. All these parts were concurrently designed *in silico* from the same personalized 3D image, subsequently 3D printed and assembled into one object, to be surgically placed in one step within the originating mandibular defect.

Data availability statement

The raw data supporting the conclusions of this article will be made available by the authors, without undue reservation.

Author contributions

Project conception (NIM, CTB); experimental work (JD, RC, DR, NIM); computer modelling (CBA, LS, NIM); manuscript preparation (NIM, JD, LS, CBA, CTB, RC). All authors contributed to the article and approved the submitted version.

Funding

This work was supported the Small Project in Rehabilitation Research (SPiRE) Award # 5I21RX003469 from the United States (U.S.) Department of Veterans Affairs, Rehabilitation Research and Development Service, and with the use of facilities at the Richard L. Roudebush VA Medical Center, Indianapolis, IN. The contents do not represent the views of the U.S. Department of Veterans Affairs or the United States Government.

Acknowledgments

The authors wish to thank Indiana Institute for Medical Research at Richard L. Roudebush VA Medical Center, Indianapolis, IN for its support to the 3D Tissue Bioprinting Core Laboratory, and Leni Moldovan for help with preparation of the figures.

Conflict of interest

The authors declare that the research was conducted in the absence of any commercial or financial relationships that could be construed as a potential conflict of interest.

Publisher's note

All claims expressed in this article are solely those of the authors and do not necessarily represent those of their affiliated organizations, or those of the publisher, the editors and the reviewers. Any product that may be evaluated in this article, or claim that may be made by its manufacturer, is not guaranteed or endorsed by the publisher.

Supplementary material

The Supplementary Material for this article can be found online at: https://www.frontiersin.org/articles/10.3389/fdmed.2022.1066501/full#supplementary-material.

References

1. Petite H, Viateau V, Bensaïd W, Meunier A, de Pollak C, Bourguignon M, et al. Tissue-engineered bone regeneration. *Nat Biotechnol*. (2000) 18:959–63. doi: 10.1038/79449

2. Liu M, Lv Y. Reconstructing bone with natural bone graft: a review of in vivo studies in bone defect animal model. *Nanomaterials (Basel)*. (2018) 8:999. doi: 10.3390/nano8120999

3. Singh N, Dhiman RK, Kumar D. Prosthodontic rehabilitation of extraoral and intraoral maxillofacial defects. *Med J Armed Forces India*. (2015) 71:S556–9. doi: 10.1016/j.mjafi.2014.02.004

4. Joda T, Gallucci GO, Wismeijer D, Zitzmann NU. Augmented and virtual reality in dental medicine: a systematic review. *Comput Biol Med*. (2019) 108:93–100. doi: 10.1016/j.compbiomed.2019.03.012

5. Canady JW, Zeitler DP, Thompson SA, Nicholas CD. Suitability of the iliac crest as a site for harvest of autogenous bone grafts. *Cleft Palate Craniofac J*. (1993) 30:579–81. doi: 10.1597/1545-1569_1993_030_0579_sotica_2.3.co_2

6. Zamiri B, Shahidi S, Eslaminejad MB, Khoshzaban A, Gholami M, Bahramnejad E, et al. Reconstruction of human mandibular continuity defects with allogenic scaffold and autologous marrow mesenchymal stem cells. *J Craniofac Surg*. (2013) 24:1292–7. doi: 10.1097/SCS.0b013e318294288a

7. Tatara AM, Koons GL, Watson E, Piepergerdes TC, Shah SR, Smith BT, et al. Biomaterials-aided mandibular reconstruction using in vivo bioreactors. *Proc Natl Acad Sci USA*. (2019) 116:6954–63. doi: 10.1073/pnas.1819246116

8. Stoop CC, Chatzivasileiou K, Berkhout WER, Wismeijer D. Marginal and internal fit of 3D printed resin graft substitutes mimicking alveolar ridge augmentation: an in vitro pilot study. *PLoS One*. (2019) 14:e0215092. doi: 10.1371/journal.pone.0215092

9. Bartnikowski M, Vaquette C, Ivanovski S. Workflow for highly porous resorbable custom 3D printed scaffolds using medical grade polymer for large volume alveolar bone regeneration. *Clin Oral Implants Res*. (2020) 31:431–41. doi: 10.1111/clr.13579

10. Anderson M, Dubey N, Bogie K, Cao C, Li J, Lerchbacker J, et al. Three-dimensional printing of clinical scale and personalized calcium phosphate scaffolds for alveolar bone reconstruction. *Dent Mater*. (2022) 38:529–39. doi: 10.1016/j.dental.2021.12.141

11. Kunrath MF. Customized dental implants: manufacturing processes, topography, osseointegration and future perspectives of 3D fabricated implants. *Bioprinting*. (2020) 20:e00107. doi: 10.1016/j.bprint.2020.e00107

12. Twohig C, Helsinga M, Mansoorifar A, Athirasala A, Tahayeri A, França CM, et al. A dual-ink 3D printing strategy to engineer pre-vascularized bone scaffolds in-vitro. *Mater Sci Eng C Mater Biol Appl*. (2021) 123:111976. doi: 10.1016/j.msec.2021.111976

13. Carrel JP, Wiskott A, Scherrer S, Durual S. Large bone vertical augmentation using a three-dimensional printed TCP/HA bone graft: a pilot study in dog mandible. *Clin Implant Dent Relat Res*. (2016) 18:1183–92. doi: 10.1111/cid.12394

14. Carrel JP, Wiskott A, Moussa M, Rieder P, Scherrer S, Durual S. A 3D printed TCP/HA structure as a new osteoconductive scaffold for vertical bone augmentation. *Clin Oral Implants Res*. (2016) 27:55–62. doi: 10.1111/clr.12503

15. Mousa M, Carrel J-P, Scherrer S, Cattani-Lorente M, Wiskott A, Durual S. Medium-term function of a 3D printed TCP/HA structure as a new osteoconductive scaffold for vertical bone augmentation: a simulation by BMP-2 activation. *Materials (Basel)*. (2015) 8:2174–90. doi: 10.3390/ma8052174

16. Muallah D, Sembdner P, Holtzhausen S, Meissner H, Hutsky A, Ellmann D, et al. Adapting the pore size of individual, 3D-printed CPC scaffolds in maxillofacial surgery. *J Clin Med*. (2021) 10:2654. doi: 10.3390/jcm10122654

17. Paxton N, Smolan W, Böck T, Melchels F, Groll J, Jungst T. Proposal to assess printability of bioinks for extrusion-based bioprinting and evaluation of rheological properties governing bioprintability. *Biofabrication*. (2017) 9:044107. doi: 10.1088/1758-5090/aa8dd8

18. Hinton TJ, Jallerat Q, Palchesko RN, Park JH, Grodzicki MS, Shue HJ, et al. Three-dimensional printing of complex biological structures by freeform reversible embedding of suspended hydrogels. *Sci Adv*. (2015) 1:e1500758. doi: 10.1126/sciadv.1500758

19. Bhattacharjee T, Zehnder SM, Rowe KG, Jain S, Nixon RM, Sawyer WG, et al. Writing in the granular gel medium. *Sci Adv*. (2015) 1:e1500655. doi: 10.1126/sciadv.1500655

20. Dairaghi J, Rogozea D, Cadle R, Bustamante J, Moldovan L, Petrache HI, et al. 3D Printing of human ossicle models for the biofabrication of personalized middle ear prostheses. *Appl Sci*. (2022) 12:11015. doi: 10.3390/app122111015

21. Crica LE, Wengenroth J, Tiainen H, Ionita M, Haugen HJ. Enhanced x-ray absorption for micro-CT analysis of low density polymers. *J Biomater Sci Polym Ed*. (2016) 27:805–23. doi: 10.1080/09205063.2016.1152856

22. Broder JS. *Diagnostic imaging for the emergency physician E-book*. Philadelphia, PA: Elsevier Health Sciences (2011).

23. Woodmansey KF, Ayik M, Buschang PH, White CA, He J. Differences in masticatory function in patients with endodontically treated teeth and single-implant–supported prostheses: a pilot study. *J Endod*. (2009) 35:10–4. doi: 10.1016/j.joen.2008.10.016

24. Khan AA, McCreary B, Owatz CB, Schindler WG, Schwartz SA, Keiser K, et al. The development of a diagnostic instrument for the measurement of mechanical allodynia. *J Endod*. (2007) 33:663–6. doi: 10.1016/j.joen.2006.06.003

25. Sakuraba M, Miyamoto S, Fujiki M, Higashino T, Oshima A, Hayashi R. Analysis of functional outcomes in patients with mandible reconstruction using vascularized fibular grafts. *Microsurgery*. (2017) 37:101–4. doi: 10.1002/micr.22433

26. Xu N, Ye X, Wei D, Zhong J, Chen Y, Xu G, et al. 3D Artificial bones for bone repair prepared by computed tomography-guided fused deposition modeling for bone repair. *ACS Appl Mater Interfaces*. (2014) 6:14952–63. doi: 10.1021/am502716t

27. Parrado-Agudelo JZ, Narváez-Tovar C. Mechanical characterization of polylactic acid, polycaprolactone and lay-fomm 40 parts manufactured by fused deposition modeling, as a function of the printing parameters. *Iteckne*. (2019) 16:111–7. doi: 10.15332/iteckne.v16i2.2354

28. Aho J, Bøtker JP, Genina N, Edinger M, Arnfast L, Rantanen J. Roadmap to 3D-printed oral pharmaceutical dosage forms: feedstock filament properties and characterization for fused deposition modeling. *J Pharm Sci*. (2019) 108:26–35. doi: 10.1016/j.xphs.2018.11.012

29. Edranov SS, Matveeva NY, Kalinichenko SG. Osteogenic and regenerative potential of free gingival graft. *Bull Exp Biol Med*. (2021) 171:404–8. doi: 10.1007/s10517-021-05237-w

30. Kitagawa T, Tanimoto Y, Nemoto K, Aida M. Influence of cortical bone quality on stress distribution in bone around dental implant. *Dent Mater J*. (2005) 24:219–24. doi: 10.4012/dmj.24.219

31. Cicciù M, Bramanti E, Cecchetti F, Scappaticci L, Guglielmino E, Risitano G. FEM and Von Mises analyses of different dental implant shapes for masticatory loading distribution. *Oral Implantol (Rome)*. (2014) 7:1–10.

32. Khalaf AT, Wei Y, Wan J, Zhu J, Peng Y, Abdul Kadir SY, et al. Bone tissue engineering through 3D bioprinting of bioceramic scaffolds: a review and update. *Life (Basel)*. (2022) 12:903. doi: 10.3390/life12060903

33. Salinas AJ, Vallet-Regí M. Bioactive ceramics: from bone grafts to tissue engineering. *RSC Adv*. (2013) 3:11116–31. doi: 10.1039/c3ra00166k

34. Jodati H, Yılmaz B, Evis Z. A review of bioceramic porous scaffolds for hard tissue applications: effects of structural features. *Ceram Int*. (2020) 46:15725–39. doi: 10.1016/j.ceramint.2020.03.192

35. Lin K, Sheikh R, Romanazzo S, Roohani I. 3D Printing of bioceramic scaffolds—barriers to the clinical translation: from promise to reality, and future perspectives. *Materials (Basel)*. (2019) 12:2660. doi: 10.3390/ma12172660

36. Abbas Z, Dapporto M, Tampieri A, Sprio S. Toughening of bioceramic composites for bone regeneration. *J Compos Sci*. (2021) 5:259. doi: 10.3390/jcs5100259

37. Dorozhkin SV. Bioceramics of calcium orthophosphates. *Biomaterials*. (2010) 31:1465–85. doi: 10.1016/j.biomaterials.2009.11.050

38. Bartnikowski M, Dargaville TR, Ivanovski S, Hutmacher DW. Degradation mechanisms of polycaprolactone in the context of chemistry, geometry and environment. *Prog Polym Sci*. (2019) 96:1–20. doi: 10.1016/j.progpolymsci.2019.05.004

39. Lam CX, Hutmacher DW, Schantz JT, Woodruff MA, Teoh SH. Evaluation of polycaprolactone scaffold degradation for 6 months in vitro and in vivo. *J Biomed Mater Res A*. (2009) 90:906–19. doi: 10.1002/jbm.a.32052

40. Sun H, Mei L, Song C, Cui X, Wang P. The in vivo degradation, absorption and excretion of PCL-based implant. *Biomaterials*. (2006) 27:1735–40. doi: 10.1016/j.biomaterials.2005.09.019

41. Lam CX, Savalani MM, Teoh S-H, Hutmacher DW. Dynamics of in vitro polymer degradation of polycaprolactone-based scaffolds: accelerated versus simulated physiological conditions. *Biomed Mater*. (2008) 3:034108. doi: 10.1088/1748-6041/3/3/034108

42. Roberts TT, Rosenbaum AJ. Bone grafts, bone substitutes and orthobiologics: the bridge between basic science and clinical advancements in fracture healing. *Organogenesis*. (2012) 8:114–24. doi: 10.4161/org.23306

43. Gonzalez-Fernandez T, Tenorio AJ, Campbell KT, Silva EA, Leach JK. Alginate-based bioinks for 3D bioprinting and fabrication of anatomically accurate bone grafts. *Tissue Eng Part A*. (2021) 27:1168–81. doi: 10.1089/ten.TEA.2020.0305

44. Barceló X, Eichholz KF, Garcia O, Kelly DJ. Tuning the degradation rate of alginate-based bioinks for bioprinting functional cartilage tissue. *Biomedicines*. (2022) 10:1621. doi: 10.3390/biomedicines10071621

45. Ahlfeld T, Lode A, Richter RF, Pradel W, Franke A, Rauner M, et al. Toward biofabrication of resorbable implants consisting of a calcium phosphate cement and fibrin-A characterization in vitro and in vivo. *Int J Mol Sci*. (2021) 22:1218. doi: 10.3390/ijms22031218

46. Kilian D, Sembdner P, Bretschneider H, Ahlfeld T, Mika L, Lützner J, et al. 3D Printing of patient-specific implants for osteochondral defects: workflow for an MRI-guided zonal design. *Bio-Des Manuf*. (2021) 4:818–32. doi: 10.1007/s42242-021-00153-4

47. Safonov A, Maltsev E, Chugunov S, Tikhonov A, Konev S, Evlashin S, et al. Design and fabrication of complex-shaped ceramic bone implants via 3d printing based on laser stereolithography. *Appl Sci*. (2020) 10:7138. doi: 10.3390/app10207138

48. Zhang W, Shi W, Wu S, Kuss M, Jiang X, Untrauer JB, et al. 3D Printed composite scaffolds with dual small molecule delivery for mandibular bone regeneration. *Biofabrication*. (2020) 12:035020. doi: 10.1088/1758-5090/ab906e

49. Brown WE, Huang BJ, Hu JC, Athanasiou KA. Engineering large, anatomically shaped osteochondral constructs with robust interfacial shear properties. *NPJ Regen Med*. (2021) 6:42. doi: 10.1038/s41536-021-00152-0

50. Ahlfeld T, Akkineni AR, Förster Y, Köhler T, Knaack S, Gelinsky M, et al. Design and fabrication of Complex scaffolds for bone defect healing: combined 3D plotting of a calcium phosphate cement and a growth factor-loaded hydrogel. *Ann Biomed Eng*. (2017) 45:224–36. doi: 10.1007/s10439-016-1685-4

51. Roque R, Barbosa GF, Guastaldi AC. Design and 3D bioprinting of interconnected porous scaffolds for bone regeneration. An additive manufacturing approach. *J Manuf Process*. (2021) 64:655–63. doi: 10.1016/j.jmapro.2021.01.057

52. Noble C, Maxson EL, Lerman A, Young MD. Mechanical and finite element evaluation of a bioprinted scaffold following recellularization in a rat subcutaneous model. *J Mech Behav Biomed Mater*. (2020) 102:103519. doi: 10.1016/j.jmbbm.2019.103519

53. Kunrath MF, Hubler R, Silva RM, Barros M, Teixeira ER, Correia A. Influence of saliva interaction on surface properties manufactured for rapid osseointegration in dental implants. *Biofouling*. (2021) 37:757–66. doi: 10.1080/08927014.2021.1964487

54. Moss SM, Ortiz-Hernandez M, Levin D, Richburg CA, Gerton T, Cook M, et al. A biofabrication strategy for a custom-shaped, non-synthetic bone graft precursor with a prevascularized tissue shell. *Front Bioeng Biotechnol*. (2022) 10:838415. doi: 10.3389/fbioe.2022.838415

55. Hu J, Wang JH, Wang R, Yu XB, Liu Y, Baur DA. Analysis of biomechanical behavior of 3D printed mandibular graft with porous scaffold structure designed by topological optimization. *3D Print Med*. (2019) 5:5. doi: 10.1186/s41205-019-0042-2

56. Colnot C, Zhang X, Knothe Tate ML. Current insights on the regenerative potential of the periosteum: molecular, cellular, and endogenous engineering approaches. *J Orthop Res*. (2012) 30:1869–78. doi: 10.1002/jor.22181

57. Zhang W, Wang N, Yang M, Sun T, Zhang J, Zhao Y, et al. Periosteum and development of the tissue-engineered periosteum for guided bone regeneration. *J Orthop Translat*. (2022) 33:41–54. doi: 10.1016/j.jot.2022.01.002

58. Garner J, Davidson D, Eckert GJ, Barco CT, Park H, Park K. Reshapable polymeric hydrogel for controlled soft-tissue expansion: in vitro and in vivo evaluation. *J Control Release*. (2017) 262:201–11. doi: 10.1016/j.jconrel.2017.07.029

59. Barwinska D, Garner J, Davidson DD, Cook TG, Eckert GJ, Tholpady SS, et al. Mucosal perfusion preservation by a novel shapeable tissue expander for oral reconstruction. *Plast Reconstr Surg Glob Open*. (2017) 5:e1449. doi: 10.1097/GOX.0000000000001449

60. Garner J, Davidson DD, Barwinska D, Eckert GJ, Tholpady SS, Park K, et al. Reshapable hydrogel tissue expander for ridge augmentation: results of a series of successive insertions at the same intraoral site. *J Periodontol*. (2019) 90:718–27. doi: 10.1002/JPER.18-0629

61. Lee S, Choi D, Shim JH, Nam W. Efficacy of three-dimensionally printed polycaprolactone/beta tricalcium phosphate scaffold on mandibular reconstruction. *Sci Rep*. (2020) 10:4979. doi: 10.1038/s41598-020-61944-w

62. Ahlfeld T, Doberenz F, Kilian D, Vater C, Korn P, Lauer G, et al. Bioprinting of mineralized constructs utilizing multichannel plotting of a self-setting calcium phosphate cement and a cell-laden bioink. *Biofabrication*. (2018) 10:045002. doi: 10.1088/1758-5090/aad36d

63. Ahlfeld T, Schuster FP, Forster Y, Quade M, Akkineni AR, Rentsch C, et al. 3D Plotted biphasic bone scaffolds for growth factor delivery: biological characterization in vitro and in vivo. *Adv Healthc Mater*. (2019) 8:e1801512. doi: 10.1002/adhm.201801512

64. Dudukovic NA, Fong EJ, Gemeda HB, DeOtte JR, Cerón MR, Moran BD, et al. Cellular fluidics. *Nature*. (2021) 595:58–65. doi: 10.1038/s41586-021-03603-2

65. Renders GA, Mulder L, van Ruijven LJ, van Eijden TM. Porosity of human mandibular condylar bone. *J Anat*. (2007) 210:239–48. doi: 10.1111/j.1469-7580.2007.00693.x

66. Meyer C, Kahn J-L, Boutemi P, Wilk A. Photoelastic analysis of bone deformation in the region of the mandibular condyle during mastication. *J Cranio-Maxillofac Surg*. (2002) 30:160–9. doi: 10.1054/jcms.2002.0297

67. Huiskes R, Weinans H, Van Rietbergen B. The relationship between stress shielding and bone resorption around total hip stems and the effects of flexible materials. *Clin Orthop Relat Res*. (1992) 274:124–34.